Multigrid spatially constrained dispersion curve inversion: towards distributed acoustic sensing surface wave imaging

Jianbo Guan[1], Feng Cheng[1,2*], Jianghai Xia[1], Binbin Mi[1], Haoyuan Sun[1], and Jonathan B. Ajo-Franklin[2,3]

[1]Key Laboratory of Geoscience Big Data and Deep Resource of Zhejiang Province, School of Earth Sciences, Zhejiang University, 866 Yuhangtang Rd., Hangzhou, Zhejiang 310027, China
[2]Dept. of Earth, Environmental, and Planetary Sciences, Rice University, 6100 Main St., Houston, TX 77005, USA
[3]Lawrence Berkeley National Laboratory, 1 Cyclotron Rd., Berkeley, CA 94720, USA

Key Points:

- We formulated a multigrid spatially constrained inversion scheme for holistic inversion of surface wave dispersion curves.
- We demonstrated the robustness and effectiveness of the proposed method, especially in the context of high-resolution DAS surface wave imaging.
- We refined a high resolution S-wave velocity model, uncovering new insights into understanding the fault system in Imperial Valley.

Corresponding author: Feng Cheng, `fengcheng@zju.edu.cn`

Abstract

Surface wave methods, commonly applied in diverse fields, encounter challenges in complex subsurface environments due to limitations inherent in traditional inversion techniques. Conventional one-dimensional inversion (1DI), with its reliance on fixed grids and deterministic linear approaches, often introduces biases, diminishing lateral resolution. Laterally constrained inversion (LCI) improves robustness by addressing lateral coherency but falls short in delineating arbitrary interfaces due to its dependency on fixed grid models. The advent of Distributed Acoustic Sensing (DAS) technology offers extensive seismic data, yet its potential for high-resolution imaging remains underutilized. We introduce a Multigrid Spatially Constrained Dispersion Curve Inversion (MCI) method to overcome these challenges, aiming to harness high-resolution DAS surface wave imaging capabilities. This paper details the MCI scheme, evaluates its efficacy through synthetic tests, and applies it to a DAS field study in Imperial Valley, California. Our findings demonstrate a refined, higher-resolution S-wave velocity model, offering new insights into the region's fault system and emphasizing the necessity of improved spatial resolution in large-scale geophysical studies.

Plain Language Summary

Studying what is beneath the Earth's surface can be tricky because of how complex it is. One common method involves analyzing surface waves, but this has its own challenges. The usual way to interpret the data, called one-dimensional inversion (1DI), can introduce errors and not give a clear picture. Recently proposed alternatives like laterally constrained inversion (LCI) also have limitations, especially when dealing with a new type of seismic data called distributed acoustic sensing (DAS). To overcome these limitations, we present a promising solution called Multigrid Spatially Constrained Dispersion Curve Inversion (MCI). This method enhances our ability to visualize what lies beneath the surface with greater clarity and detail. We have conducted tests using synthetic data and applied MCI in a public DAS dataset collected from a ∼28-km-long existing unused telecommunication fiber in Imperial Valley, CA. The results give us a better understanding of the underground faults in the region and show that improving how we see things below ground is crucial for large-scale studies.

1 Introduction

Shear-wave velocity (V_s) is an important indicator to assess the physical and mechanical parameters of the subsurface material (Ayres & Theilen, 1999; Abd Rahman et al., 2023; Sawayama et al., 2022). Seismic surface waves, which contain rich information on the material considered, are widely used in estimating structures at different scales from the near surface to upper mantle (Xia et al., 1999; Shapiro & Ritzwoller, 2002). The classical surface wave method, by performing dispersion analysis and inversion on either active-source or passive-source seismic data, is able to predict the local depth-dependent profile (Xia et al., 1999; Park & Miller, 2008). With the benefits of noninvasiveness, effectiveness, and robustness, this method is increasingly utilized in near-surface geophysics, geotechnical engineering, and exploration geophysics, as well as environmental geology and hydrogeology. Surface wave approaches have been widely applied to study problems as diverse as urban subsurface space investigation (Kühn et al., 2011; Wang et al., 2023), site effect estimation (Foti et al., 2009; Kanbur et al., 2020; Cheng, Ajo-Franklin, & Tribaldos, 2023), archaeology (Mecking et al., 2021; Guan et al., 2022), resource exploration (Ajo-Franklin et al., 2022; Cheng, Ajo-Franklin, Nayak, et al., 2023), environmental and groundwater monitoring (Sens-Schönfelder & Wegler, 2006; Bergamo et al., 2016; Mi et al., 2020), geological hazards early warning (Bazin et al., 2010; Foti et al., 2011; Bottelin et al., 2013; Salas-Romero et al., 2021).

The commonly employed surface wave inversion method typically involves two steps. Initially, utilizing a series of fixed vertical discrete grids, a deterministic linear inversion algorithm is applied to individually invert the measured dispersion curves and produce 1D layered V_s profiles at respective locations. Subsequently, the neighboring 1D profiles are assembled through horizontal interpolation to create the final pseudo-2D/3D velocity structure. However, dispersion curve inversion is typically an ill-posed optimization problem with non-unique solutions. Furthermore, taking into account the inevitable irregular spatial sampling during data acquisition and possible lateral variations of the underground structure, this two-step procedure has the drawback of generating a biased velocity model by introducing artifacts and obscuring the lateral resolution (Strobbia & Foti, 2006; Lin & Lin, 2007; Mi et al., 2017). These limitations impede the progress of the surface wave method in scenarios involving complex underground structures, such as geotechnical characterization and active fault identification.

Regularization techniques are capable of improving the robustness of deterministic inversion and constraining the suitability and uniqueness of the solution (Tikhonov, 1963; Zhdanov, 2002). For example, constrained inversion methods based on regularization of the minimum gradient norm have been developed to minimize the roughness of the model and alleviate the effect of lateral ambiguities (Xia et al., 1999; Herrmann & Ammon, 2002; Wisén & Christiansen, 2005; Cercato, 2007, 2009; Socco et al., 2009; Haney & Qu, 2010; Vignoli et al., 2012, 2021; Bergamo et al., 2016; Dokht Dolatabadi Esfahani et al., 2020; Hu et al., 2021; Guillemoteau et al., 2022; Cruz-Hernández et al., 2022). Inspired by the laterally constrained inversion (LCI) approach to analyze resistivity data, (Auken & Christiansen, 2004), Wisén and Christiansen (2005) and Socco et al. (2009), proposed to apply the LCI scheme for surface wave dispersion curve inversion based on L2-norm regularization. Taking into account lateral coherency, this class of methods simultaneously inverts multiple dispersion curves and updates all of the corresponding 1D models to directly construct a pseudo-2D/3D model. Haney and Qu (2010) compared the inversion results from L2 and L1 norm regularization and concluded that the latter better recovers layered structures due to its weaker penalty on sharp contrasts, which allows a wider distribution of target parameters. Guillemoteau et al. (2022) introduced the minimum gradient-supported stabilizer into the LCI method and discussed the feasibility of controlling the sharpness of the interfaces by tuning a focusing factor. However, two major problems still exist: first, the LCI method tends to delineate target structures with blocky boundaries (i.e., either vertical or horizontal), rather than the true arbitrary interface; second, the LCI method is still based on a fixed grid model, the same as the 1D inversion method, and the accuracy of the depth inversion relies on the prior model parameterization, which highly depends on the experience of the interpreter. Instead of utilizing fixed grids, stochastic algorithms have been developed, for example, classical genetic algorithms (Shi & Jin, 1995), simulated annealing (Beaty et al., 2002), and particle swarms (X. Song et al., 2012), to expand the model parameter space with a series of variable grid models. However, it is impractical to apply lateral constraints on thousands of possible models simultaneously, especially for large-scale surveys with hundreds or thousands of dispersion curves to be inverted.

Distributed Acoustic Sensing (DAS) is an innovative technique for high resolution seismic data acquisition, involving the demodulation of optical signals transmitted through a fiber optic cable (Posey Jr et al., 2000; Parker et al., 2014). DAS can efficiently collect ultra-large-scale datasets, covering tens of kilometers spatially with meter to submeter spatial resolution. This makes DAS increasingly relevant to geophysical field observations and monitoring, particularly in complex conditions (Lindsey et al., 2017; Ajo-Franklin et al., 2019, 2022; Lindsey et al., 2019; Walter et al., 2020; Rodríguez Tribaldos & Ajo-Franklin, 2021; Cheng et al., 2021a, 2021b, 2022). Despite the widespread use of DAS in near-surface seismic imaging, the majority of applications still rely on classical 1D surface wave inversion schemes (Ajo-Franklin et al., 2019; Cheng et al., 2021a, 2021b; Spica et al., 2020; Cheng, Ajo-Franklin, & Tribaldos, 2023; Yan et al., 2023; Z. Song

et al., 2020). This approach falls short of fully leveraging the high-resolution capabilities of DAS. Consequently, there is a pressing demand for a new generation DAS seismic imaging technique that can provide fine-scale spatial resolution across large-scale spatial coverage.

In this study, we develop a multigrid spatially constrained dispersion curve inversion (MCI) scheme to address the pressing need for high-resolution DAS surface wave imaging. The basic framework of dispersion curve inversion is first reviewed, followed by a detailed explanation of the key aspects and implementation process of MCI. The effectiveness of MCI is then evaluated through both synthetic testing and a real case involving basin-scale near-surface 2D imaging using an existing DAS dataset. Additionally, this study explores the impact of grid grouping on MCI, examines the imaging spatial resolution of the surface wave method, and discusses the potential extension of MCI to 3D imaging.

2 Methodology

2.1 Framework of dispersion curve inversion

According to Xia et al. (1999), surface wave dispersion curves are more sensitive to S-wave velocity (V_s) than P-wave velocity ((V_p)) and density (ρ). A deterministic inversion method, e.g., the Gauss-Newton algorithm, is employed to invert the dispersion curve for the 1D V_s model. The model is parameterised by discretizing the subsurface profile into a series of 1D fixed grids. To improve the convexity of the inversion, we transform model parameters and observed data into logarithmic space (Auken & Christiansen, 2004) (see Fig. S1 in Supporting Information for the comparison of sensitivity kernel with and without logarithmic parametrization). Here, observed data $\mathbf{d}$ is defined as

$$\mathbf{d} = \log(\mathbf{c}) = [\log(c_1), \ldots, \log(c_p)]^T. \tag{1}$$

where, $\mathbf{c}$ is the measured phase velocity vector; p is the length of vector $\mathbf{c}$. We assume the Poisson's ratio and density of the parameterized model $\mathbf{m}$ are homogeneous (Xia et al., 1999), and only the V_s is of interest in the inversion

$$\mathbf{m} = \log(\mathbf{V}_s) = [\log(V_{s1}), \ldots, \log(V_{sq})]^T. \tag{2}$$

where, q are the lengths of vectors $\mathbf{V}_s$.

In order to find the optimal model, the objective function ($\Phi(\mathbf{m})$), containing the observed data reproducibility as well as the regularization term, is defined and minimised

$$\begin{aligned} \Phi(\mathbf{m}) &= \phi(\mathbf{m}) + \lambda R(\mathbf{Dm}) \\ &= \|\mathbf{W}_d(\mathbf{d} - F(\mathbf{m}))\|_2^2 + \lambda R(\mathbf{Dm}); \end{aligned} \tag{3}$$

where, $\phi(\mathbf{m})$ is the data residual; $\| \ \|_2$ represents the L2-norm calculation; F is the forward kernel of the surface wave dispersion curve based on 1D elastic layered model (Haskell, 1953); $\mathbf{W}_d$ is a diagonal matrix, which is the product of the reciprocal of data uncertainties and frequency/wavelength weights (Socco et al., 2009; Hu et al., 2021); λ is the trade-off coefficient that balances the contribution weights between the data residual term and the model regularization term, and is adaptively determined during the inversion (Zhdanov, 2002); $\mathbf{D}$ is the spatial gradient matrix, which consists of the differential coefficients between each cell of the grid and its surrounding ones. R is an updated L2-norm regularization in Occam-type (Portniaguine & Zhdanov, 1999). Instead of focusing on the amount of parameter variation, here R tends to minimize the distribution of parameter discontinuities

$$R(\mathbf{Dm}) = \frac{\|\mathbf{Dm}\|_2^2}{\|\mathbf{Dm}\|_2^2 + \nu^2}, \tag{4}$$

where ν is the focusing factor to avoid singularities when the numerator term is approaching zero (Porcella, 1984). Generally, a small ν would sharpen the interface, but there is

a risk that overfitting would occur and the solution could be unrealistic. After some trial and error, we realized that there will be a good balance between sharpness and reasonableness of the solution when ν is around 0.01. In the following synthetic and field tests, ν is set to 0.01.

To minimize the objective function ($\Phi(\mathbf{m})$), an iterative update strategy is applied, and the update direction ($\delta\mathbf{m}$) of the current iteration is determined by using the conjugate gradient least squares method (Golub & Van Loan, 2013),

$$[\mathbf{J}^T\mathbf{W}_d^T\mathbf{W}_d\mathbf{J} + \lambda\mathbf{D}^T\mathbf{W}_m\mathbf{D}]\delta\mathbf{m} = \mathbf{J}^T\mathbf{W}_d^T\mathbf{W}_d[\mathbf{d} - f(\mathbf{m}')] - \mathbf{D}^T\mathbf{W}_m\mathbf{D}\mathbf{m}', \tag{5}$$

where, $\mathbf{m}'$ is the previously updated model, and the current updated model can be presented as $\mathbf{m} = \mathbf{m}' + \delta\mathbf{m}$; $\mathbf{J}$ is the Jacobin matrix in logarithmic space; $\mathbf{W}_m$ is a diagonal matrix used to ensure the stability of the linear system (Farquharson, 2008). The iteration will terminate when the defined threshold of data residual or the maximum number of iterations is exceeded.

Based on the above framework, the classic 1D inversion scheme (1DI) and LCI scheme of dispersion curve inversion can be simply implemented. For example, in the 1DI case, $\mathbf{d}$ and $\mathbf{m}$ represent the measured dispersion curve and the inverted 1D model for a single site, respectively; while in the LCI case, they represent the measured dispersion curves and the corresponding 1D models for all sites, respectively. In addition, in the 1DI case, only variations between vertical layers ($\mathbf{D}_z$) are constrained

$$\mathbf{D} = \mathbf{D}_z; \tag{6}$$

while in the LCI case, the lateral coherency between neighboring 1D models ($\mathbf{D}_x$) is also taken into account

$$\mathbf{D} = [\mathbf{D}_z, \gamma_x\mathbf{D}_x]^T \tag{7}$$

where, γ_x represents the weight of constraint in the x direction and can be determined using the strategy described in Guillemoteau et al. (2022).

2.2 Multigrid spatially constrained inversion

While the existing framework for dispersion curve inversion has been widely utilized to image subsurface V_s structures across various scales, it encounters significant challenges in meeting the high-resolution demands of modern dense nodal and DAS arrays. The primary issue lies in the reliance of the framework on predefined models with fixed grids. The inverted V_s at each grid cell is actually an average of the corresponding velocity units around the cell. This can obscure the target discontinuity interface and limit the vertical resolution. Furthermore, the rigidity of fixed grid models complicates efforts to address the inherent non-uniqueness in 2D/3D dispersion curve inversion solutions.

Another limitation is spatial constraints of the existing framework, which are typically limited to vertical and/or horizontal directions. This constraint system tends to exaggerate anomalies that align vertically or horizontally but fails to adequately represent anomalies with irregularly shaped boundaries.

To address these challenges, we propose a multigrid spatially constrained inversion (MCI) framework tailored for 2D dispersion curve inversion, with a particular focus on DAS surface wave inversion. This innovative framework is also adaptable for 3D surface wave inversion challenges, which will be further discussed in section 5.3. It's important to note that while our proposed MCI approach builds upon the classical dispersion curve forward kernel (e.g., Haskell, 1953; Knopoff, 1964; Chen, 1993), which assumes horizontal stratification, it also holds the potential for integration with other forward kernels (e.g., Hu et al., 2021; Y. Liu et al., 2023).

2.2.1 Multigrid parameterization strategy

Inspired by the multigrid scheme applied in the seismic tomography community (Thurber, 1983; Vesnaver & Böhm, 2000; Arato et al., 2014; Tong et al., 2019; Luo et al., 2021), we adopt a multigrid model parameterization strategy to deal with the aforementioned problems associated with the fixed grid model.

In our 2D dispersion curve inversion approach, we discretize the subsurface structure into a series of vertically oriented 1D grids, all of a uniform scale. Following the methodology outlined by Tong et al. (2019), we define a set of multigrid models that include a base grid and several collocated grids (Fig. 2). The base grid is composed of uniformly sized cells, as small as practicable to meet our desired resolution requirements. In contrast, the collocated grids feature cells of varying sizes. This variation in cell scales across the collocated grids enables more effective spatial boundary constraints through multiple samplings of target units and helps reduce solution non-uniqueness by expanding the model space. The cell sizes in these collocated grids are larger than those in the base grid and increase progressively with depth to accommodate the diminishing resolution of surface waves and to optimize computational efficiency.

Our inversion process involves several steps in each iteration. Initially, the model is projected from the base grid to each collocated grid. Then, the model for each collocated grid is updated and backprojected onto the base grid independently. After this, all updated models are averaged to update the base grid model and assess the optimization process (Fig. 2). Consequently, the inversion is executed on each collocated grid, while the solution evaluation occurs on the base grid.

To ensure that the high-quality models from the collocated grids are adequately represented, the base grid model $\mathbf{m}$ is updated through a weighted averaging process. This weighting is based on the data residual of each collocated grid model, thus adaptively increasing the contribution from models with lower residuals.

$$\begin{aligned}\mathbf{m} &= \sum_{i=1}^{G} \alpha_i * \mathbf{m}_i \\ &= \sum_{i=1}^{G} \frac{\phi(\mathbf{m}_i)^{-1}}{\sum \phi(\mathbf{m}_i)^{-1}} * \mathbf{m}_i,\end{aligned} \tag{8}$$

where, G is the number of collocated grids, $\mathbf{m}_i$ is the i-th collocated-grid model, $\alpha_i = \phi(\mathbf{m}_i)^{-1} / \sum \phi(\mathbf{m}_i)^{-1}$ represents the data residual weight of the i-th collocated-grid model.

Equation 8 plays a pivotal role in the multigrid model by guiding the update direction and preventing convergence to local extremes. This approach, when contrasted with the single grid model, endows the multigrid model with reduced uncertainty and enhanced robustness during the inversion process. Theoretically, the variance inherent in the multigrid model is estimated to be approximately $1/G$ times that of a single grid model (Tong et al., 2019; Luo et al., 2021), which indicates that the solution of the multigrid model is likely to be closer to the true model, providing a more accurate representation.

Moreover, the multigrid strategy offers an effective method for quantifying the uncertainty of inversion results related to parameterization of the 2D dispersion curve inversion process. This is achieved by computing the standard deviation (σ) between the models derived from the collocated grids and the base grid,

$$\sigma = \sqrt{\frac{\sum_{i=1}^{G} (\mathbf{m}_i - \mathbf{m})^2}{G}}. \tag{9}$$

The ability to accurately gauge uncertainty is a significant advantage of the multigrid approach, particularly in complex inversion scenarios where precision is paramount. Such

a quantitative assessment of uncertainty is crucial for evaluating the reliability of the inversion outcomes. It is important to note that the effectiveness of this uncertainty assessment is closely linked to how the collocated grids are defined, as discussed by (Luo et al., 2021). The number of grids and the degree of their randomization play a significant role in this context. Typically, employing a greater number of grids with higher levels of randomization introduces a broader range of perspectives in the model, thereby providing a more comprehensive evaluation of potential variability and uncertainty. Consequently, the strategic configuration of collocated grids is a crucial factor in leveraging the full potential of the multigrid model for reliable uncertainty assessment.

2.2.2 Multidirectional spatial regularization

Equation 7 illustrates that the spatial gradient matrices in current regularization terms predominantly incorporate difference coefficients in the vertical (z) and/or horizontal (x) directions, as noted in prior studies (e.g., Wisén & Christiansen, 2005; Socco et al., 2009; Hu et al., 2021; Guillemoteau et al., 2022). However, this approach has its drawbacks, particularly in terms of exaggerating interfaces that are either horizontal or vertical. This can lead to the formation of unrealistic, blocky anomalies in the final inverted Vs structure, a concern highlighted in (Auken & Christiansen, 2004). This issue becomes especially critical in scenarios where sloping boundaries are anticipated, potentially leading to significant inaccuracies.

To address this challenge and effectively constrain anomalies with boundaries of arbitrary shapes, we introduce a novel approach involving multidirectional spatial regularization. This includes incorporating difference coefficients in diagonal directions, providing a more nuanced and accurate representation of subsurface structures (see Fig. S2 in Supporting Information for the schematic comparison between single and multidirectional regularization). For the 2D case, we can represent the spatial gradient matrix as

$$\mathbf{D} = [\mathbf{D}_z, \gamma_x \mathbf{D}_x, \gamma_{zx} \mathbf{D}_{zx}, \gamma_{xz} \mathbf{D}_{xz}], \tag{10}$$

where, $\mathbf{D}_{zx}$ and $\mathbf{D}_{xz}$ represent the difference coefficients in upper diagonal (zx) and lower diagonal (xz) directions, respectively; γ_{zx} and γ_{xz} represent the weight of constraint in two diagonal directions. Multidirectional spatial regularization significantly enhances the depiction of interfaces, particularly those at diagonal orientations, leading to a more accurate representation of complex subsurface structures.

2.2.3 Workflow of multigrid spatially constrained inversion

We have integrated a multigrid parameterization strategy and multidirectional spatial regularization into the established dispersion curve inversion framework, culminating in the multigrid spatially constrained inversion (MCI) scheme for 2D surface wave imaging. The essence of MCI is simultaneously updating multiple collocated-grid models using multidirectional spatial regularization and adaptively averaging solutions for this family of collocated-grid models. The flowchart in Fig.2 illustrates the basic MCI workflow, which contains the following steps:

1. design a set of multigrid network, including one 2D base grid and several 2D collocated grids, for all investigation sites;
2. parameterize the base grid to establish an initial model;
3. project parameters of the initial model from the base grid to each collocated grid;
4. update each collocated-grid model using multidirectional spatial regularization (3);
5. backproject the updated model from each collocated grid to the base grid;
6. average all the backprojected models to update the inverted model at base grid;
7. repeat steps 3-6 until the termination criteria is satisfied;

8. output the last inverted model at the base grid as the final result;
9. evaluate uncertainties related to parameterization of the 2D dispersion curve inversion process by estimating the standard deviation between the final inverted model and all backprojected models at the base grid.

It is worth mentioning that it is relatively subjective to determine the number and the cell size of the collocated grids. In general, it is usually a safe option to employ a sufficient number of collocated grids with cells of various scales, although it comes with the cost of an increasing computation burden. This part will be discussed in section 5.1.

3 Synthetic test

To evaluate the performance of the multigrid spatially constrained inversion (MCI) method, we conducted synthetic tests on a pseudo-2D earth model. This model features three non-horizontal layers separated by two distinct interfaces and is represented by 61 1D models, each with identical velocity parameters but varying interlayer depths (Fig. 3a). From these models, we generated 61 phase-velocity dispersion curves as our observed data using a 1D forward kernel (Haskell, 1953). To simulate natural randomness, we introduced 4% Gaussian white noise to this data. These dispersion curves, displaying fluctuating interfaces similar to the earth model (Fig. 3b), serve as the basis for our tests. The objective is to accurately estimate the true Vs values and delineate the sharp interlayer interfaces from these noise-affected dispersion curves using the MCI method. It is worth mentioning that our synthetic tests are designed to evaluate the performance of various dispersion curve inversion algorithms, which inherently assume horizontal stratification (1D). Consequently, we have not incorporated the more ambiguous 2D forward modeling, which could introduce data uncertainties in the measurement of dispersion curves (e.g., Hu et al., 2021; Y. Liu et al., 2023).

In our synthetic tests, we first established one base grid (Grid s0) with a consistent layer thickness of 1 m. Additionally, we defined four collocated grids (Grid s1-s4), where the layer thickness varies, progressively increasing from 1 m to 2 m as the depth increases. Both the base grid and the collocated grids share the same total depth of 50 m. For ease of calculation, the layer thicknesses in the collocated grids can be set as an arithmetic series. Given the thicknesses of the first and last layers (h_1 and h_n) and the total depth (d), we can determine the thickness of each individual layer (h_i) by applying the following formula,

$$\begin{aligned} \sum_{i=1}^{n} h_i &= \frac{(h_1 + h_n) * n}{2} = d \\ h_i &= h_1 + \frac{h_n - h_1}{n-1} * (i-1). \end{aligned} \tag{11}$$

The four collocated grids (Grid s1-s4) are combined into various multigrid groups (Grid s5-s10) to assess the dependence of MCI method on collocated-grid group configurations, as detailed in Section 5.1. The thickness parameters for these grids are outlined in Table 1. Following the strategy of Xia (2014), we constructed the initial 2D Vs model (Fig. 3c) as a gradient model with horizontal layers defined by the base grid.

We applied 1DI, LCI, and MCI to the same observed data (Fig. 3b) and the initial model (Fig. 3c), ensuring meticulous grid parameterization and spatial regularization for each method. For 1DI and LCI, the initial models are projected from Grid s0 (the base grid) to Grid s1 (a single collocated grid) to maintain inversion stability. In contrast, MCI utilizes Grid s5, comprising all four collocated grids, in alignment with the multigrid requirements specified in Section 2.2.1.

Regarding spatial regularization, 1DI exclusively incorporates vertical direction constraints (eq.6). LCI extends this to include both vertical and lateral constraints (eq.7), while MCI further integrates two diagonal directions (eq.10). Following the approach recommended by Guillemoteau et al. (2022), we typically set the constraint weights to constants—specifically, 2 for the lateral direction and 1 for all other directions in this section. The optimization process is terminated either when the number of iterations surpasses 30 or when there is less than a 2% reduction in data residual between successive iterations.

The reproducibility of the observed data serves as a crucial evaluation criterion to assess the acceptability of the inversion results. In general, all three methods produce relatively low data residual with visible differences related to lateral variations (Figs. 4a1-c1). These results are acceptable considering the fact that the data contain noise. To better understand the impact of lateral variation on inversion results, we further calculate the root-mean-square relative errors (**rmsre**) for all the investigation stations. In general, 1DI and LCI yield the highest (Figs. 4a1-a2) and the lowest (Figs. 4b1-b2) data residual, respectively; while MCI produces the intermediate results and the **rmsre** curve exhibits variations associated with structural features (Figs. 4c1-c2).

Nonetheless, achieving higher reproducibility does not guarantee superior inversion results, given factors such as solution non-uniqueness, data errors, and the risk of overfitting. The conventional 1D inversion method yields suboptimal models characterized by inconsistent interlayer boundaries (Fig. 5a1) and biased halfspace velocities (Fig. 5a2). This is primarily attributed to an inappropriate initial model, which causes 1DI to converge to local extremes. In contrast, the LCI method significantly enhances the results (Fig. 5b1) by incorporating lateral constraints during the inversion process, effectively rectifying the underestimation of halfspace velocities (Fig. 5b2). It is worth noting that the sharp interfaces cannot yet be accurately depicted, resulting in a blocky reconstructed structure. This is because the LCI method amplifies the anomaly boundaries in orthogonal directions, and the predefined fixed grid limits the search space of the solution.

Built upon the multigrid spatially constrained inversion framework, the MCI method produces an optimal model (Fig. 5c1) which is highly consistent with the true model. MCI demonstrates the capability to enhance inversion robustness, and suppress blocky artifacts around sharp boundaries. It is worth mentioning that the optimal model from MCI still exhibits model residuals (Fig. 5c2). These errors stem from facts like the averaging effect of the multiple collocated grids, and the inherent limitations of the surface wave method, which has relatively weak sensitivity to high-impedance interfaces. Moreover, these model errors are closely related to the estimated uncertainties (Fig. 6). This suggests the potential to assess the reliability of the inversion in the real world by considering uncertainties during MCI.

For a fair comparison, we implement the multigrid strategy within the 1DI and LCI framework. This involves averaging the inverted models from multiple collocated grids (see Figs. S3 and S4 in Supporting Information) to generate the final model. Fig. 7 illustrates that this post-processing averaging does mitigate the blocky artifacts to some extent. However, these results are still not comparable to the outcomes of MCI. In contrast to the simultaneous multigrid averaging inherent in the MCI update iterations, this posteriori averaging relies on the limited search space of each fixed grid and lacks systematic constraints between various collocated grids.

4 Field application

4.1 Experiment and Data

The Imperial Valley, situated at the southern tip of the San Andreas Fault system, is a tectonically active basin filled with thick Quaternary alluvium and lake sediments

(Jackson, 1981; Kaspereit et al., 2016). It has experienced regular earthquakes and seismic swarms for over two decades. Accurate delineation of the shallow velocity structure across the valley is crucial for understanding seismic activity, fault systems, and assessing earthquake hazards.

The Salton Sea Seismic Imaging Project (SSIP) pioneered the first unified community velocity model for the Imperial Valley, utilizing Texan seismographs and explosive shots (Persaud et al., 2016; Ajala et al., 2019). However, the relatively sparse acquisition system limits the spatial resolution of travel-time tomography, particularly for near-surface structures. Cheng, Ajo-Franklin, and Tribaldos (2023) introduced the first high-resolution $Vs30m$ model for the valley, utilizing an existing, unused telecommunication fiber spanning approximately 28 km (the black line in Fig. 8) and a DAS surface wave imaging framework. For more details on the experiment and the region, please refer to Ajo-Franklin et al. (2022); Cheng, Ajo-Franklin, and Tribaldos (2023).

Nevertheless, the existing DAS surface wave imaging framework suffers from the limitation of employing spatial smoothing as spatial constraints, which can blur the final spatial resolution of the inverted V_s structure. In our efforts to enhance the near-surface V_s structure, we have adapted the imaging framework using our MCI method in this study. To maintain focus on the inversion algorithm itself, we have utilized the same DAS dataset as released by Cheng, Ajo-Franklin, and Tribaldos (2023). This dataset comprises 273 high-quality fundamental-mode dispersion curves (Fig. 9) extracted from 2-day DAS ambient noise data.

4.2 DAS surface wave imaging using MCI

To implement the multigrid strategy of the MCI method, we established one base grid (Grid f0) and four collocated grids (Grid f1 - f4). The maximum depth for all grids is set at 80 m. Layer thicknesses (Table . 2) are defined as suggested in the previous section. The initial V_s model featured linearly increasing velocities with depth (Fig. S5 in Supporting Information S1). Throughout the inversion process, constraint weights for all directions are uniformly set to 1. The iteration termination criteria matched those used in the synthetic test, and all three methods achieved reasonable results with data residuals (**rmsre**) generally remaining below 0.01 (see Fig. S6 in Supporting Infomation S1).

For comparison, we also conducted 1DI and LCI using the same initial model with an appropriate grid (Grid f1). The 1DI model exhibits noticeable velocity oscillations in the lateral direction, resulting in complex and difficult-to-interpret "spaghetti-like" structures (Fig. 10a). These oscillations were primarily attributed to the non-uniqueness problem stemming from an inadequate initial model and a lack of constraint information. This issue is a common challenge in surface wave imaging, and it is particularly pronounced in this study due to the high-resolution nature of DAS.

To mitigate these "spaghetti-like" features, one approach is to laterally smooth the 1DI model to enhance interpretability, as demonstrated by Cheng, Ajo-Franklin, and Tribaldos (2023). Figure 10b illustrates that this smoothing process effectively suppresses lateral velocity oscillations. However, the choice of smoothing length (0.3 km in this study, as in Cheng, Ajo-Franklin, and Tribaldos (2023)) is subjective and can potentially lead to the elimination of small-scale structures and blur the expected spatial resolution of DAS.

Another approach is to replace 1DI with LCI for a more objective representation of laterally varying structures. Figure 10c shows that LCI delineates clearer stratigraphic interfaces and preserves finer-scale local anomalies, such as soft zones at approximately 3 km and 21-22 km locations. However, a substantial proportion of the interfaces in the LCI model appears either horizontal or vertical, resulting in overly regular, "block-like"

structures. It is important to recognize that the actual subsurface structure may not conform to this rigid regularity.

In contrast, MCI excels in precisely delineating more arbitrary interfaces, as evident in the velocity contours in Figure 10c. The boundaries of the fine-scale anomalies at approximately 21-22 km locations in Figure 10c, appear more realistic. Moreover, MCI significantly reduces the abnormal jumps in data residuals of 1DI and LCI (see Fig. S6 in Supporting Information). It emphasizes the higher credibility of MCI, further supported by the generally low model uncertainties (Fig. 10e). It is worth mentioning that the notably high uncertainties around 25-26 km may be attributed to increased noise contamination in the data arising from weaker anthropogenic noise energy and stronger optical loss at greater distance. These collective observations demonstrate the remarkable robustness of the MCI method.

To evaluate the reliability of the inversion, we compare the inverted V_s models with three nearby borehole profiles, represented by the colored sticks overlaid on the 2D profiles (refer to Fig. S7 in Supporting Information for a detailed 1D comparisons). We notice a striking similarity, particularly in terms of the interfaces and average velocities. Taking account the spatial offset between observation sites, as well as the limited vertical resolution of the boreholes, we can reasonably assert the accuracy of the inverted V_s models.

We also employ the common-offset profile to further validate the resolution of MCI on revealing lateral variations. Common-offset profiles have been widely used to infer lateral stratigraphic variations with different offsets referring to different depths (Li et al., 2017, 2018; H. Liu et al., 2022; Wang et al., 2023). We compare the common-offset profile with an offset of 84 m with the inverted V_s profiles at depth of 45 m, according to the thumb rule of half-wavelength approximation. Compared to results of 1DI and LCI, MCI shows higher consistency between the local variations of V_s and that of the common-offset profile, particularly at locations around 6, 11, 22 and 25 km (indicated by the blue arrows and rectangles on Fig. 11). It demonstrates the higher spatial resolution of MCI on capturing the fine-scale local variations.

4.3 New findings from the refined V_s structure

Due to the limited resolution of the conventional 1DI, as demonstrated in Cheng, Ajo-Franklin, and Tribaldos (2023), the subsurface properties beneath 30 m exhibit a generally uniform sediment character with some concealed low-velocity zones (LVZs) near the surface. Fortunately, the high-resolution 2D V_s model, refined through the use of MCI, enhances our comprehension of the subsurface structure in Imperial Valley.

For instance, the refined model unveils two previously unidentified LVZs, one located around 3 km and the other around 21 km (Fig.10d). The northern LVZ may signify a soft paleo-depositional feature or a concealed fault located between Calipatria and Brawley, where localized discontinuities have been observed in other geophysical surveys (Meidav & Furgerson, 1972; Towse, 1975; Frith, 1978). The second LVZ, spanning approximately 1.2 km around the 21-km mark, likely represents a previously unrecognized fault zone subordinate to the deeper Brawley fault system, as revealed in (Cheng, Ajo-Franklin, Nayak, et al., 2023). This finding is corroborated by the presence of discontinuities in the common-offset profile around the 21-km location (Fig. 11), where the earlier arrivals before 0.4 s may be associated with higher overtones or wavefield oscillations within the fault zone (Ben-Zion et al., 2015).

To provide a more detailed view of this unmapped fault zone, a 5-km segment (from 19 km to 24 km) of the 2D V_s model is presented. As mentioned earlier, the 1DI model exhibits "spaghetti-like" features (Fig. 12a), hindering the interpretation of the hidden fault zone. Both the smoothed 1DI model (Fig. 12b) and the LCI model (Fig. 12c) dis-

play LVZ-like features, but they are blurred. In contrast, the MCI model distinctly preserves the boundaries of the fault zone (Fig. 12d). These new findings, relating to soft zones and potential fault systems, offer valuable insights for further research aimed at understanding seismic activity, assessing earthquake hazards, and developing sustainable energy sources in the region.

5 Discussion

5.1 Impact of Grid Grouping on Deterministic Multigrid Parameterization

The MCI framework, grounded in deterministic algorithms, entails the subjective definition of multiple collocated grids to establish a grid group for multigrid parameterization. We evaluate the influence of various grid groups (specifically, Grid s6-s10 as outlined in Table 1) featuring diverse cell sizes on MCI performance. This assessment is conducted using dispersion data and an initial model, as illustrated in Fig. 3. Grids s6-s8 each comprise two collocated grids, while Grids s9-s10 consist of three collocated grids. These grids are labeled as the fine grid, intermediate grid, coarse grid, medium-fine grid, and medium-coarse grid, categorizing them based on the degree of coarseness of the average grid cell size.

Synthetic tests reveal that the coarse grid exhibits the highest data and model residuals (Fig. 14c1-c3), while the medium-fine grid attains the lowest model residuals (Fig. 14d1-d3). The remaining grids produce comparable results. This observation implies that the grid group should include finer collocated grids to ensure the spatial resolution of MCI. However, caution is needed to avoid excessively fine collocated grids, which could lead to MCI converging to local extremes. Therefore, a thoughtful grouping of collocated grid cell scales is crucial to fully leverage the potential of MCI. We recommend determining the optimal grid group through multiple numerical tests and judiciously employing a sufficient number of collocated grids with varying scales. Typically, around 10 collocated grids are adequate to achieve a stable result.

In contrast to the deterministic inversion framework employed in this study, the stochastic inversion framework, such as the neighborhood algorithm (Sambridge, 1999) utilized in Geopsy (Wathelet et al., 2004), involves numerous individual inversions of random 1D models. It has the capability to effectively expand the model parameter space and ensure vertical resolution without incorporating multigrid parameterization. However, it is limited by its random sampling property, rendering them unable to implement multidirectional spatial regularization. Simultaneously considering spatial coherence for thousands of randomly sampled one-dimensional profiles is impractical, especially in large-scale surveys that involve the inversion of hundreds or thousands of dispersion curves.

5.2 Lateral Resolution of Surface Wave Imaging

By rolling the measured subarrays and aligning the inverted 1D V_s profiles, it is possible to reconstruct a pseudo-2D V_s structure. The horizontal resolution (δ) of surface wave imaging based on 1D forward kernel is typically associated with the geometry configurations, such as the shifting or rolling distance (r) and the subarray spread length (l) (Mi et al., 2017; Cheng, Ajo-Franklin, & Tribaldos, 2023), as illustrated in Fig. 13.

Ideally, the rolling distance represents the finest achievable imaging resolution (i.e., $\delta \geq r$), and the subarray spread length is commonly considered to be the coarsest imaging resolution (i.e., $\delta \leq l$). In practice, the primary goal for improving the resolution of the surface wave imaging algorithm is to push the lateral resolution towards the finest limitation represented by the rolling distance (r). In the case of 1DI, the lateral reso-

lution of 1DI should be close to the subarray spread length ($\delta \approx l$) due to the independence of each individual inversion. In contrast, LCI and MCI employ the spatial regularization to preserve the difference between two neighboring subarrays, resulting in their lateral resolutions being closer to the rolling distance ($\delta \approx r$). This suggests that LCI and MCI have the potential to refine the lateral resolution of surface wave imaging, given that the rolling distance is typically smaller than the subarray spread length ($r < l$).

Unfortunately, the task of configuring appropriate spatial regularization presents a challenge, as the commonly employed strategies are inherently subjective (e.g., Guillemoteau et al., 2022). Given that the spatial variations in observed data are closely related to those of the underground structure, it appears promising to regularize model constraints with spatial covariance matrix derived from data (e.g., Zhang et al., 2023). In our future work, we plan to explore the realm of joint model and data constrained inversion. This exploration aims to refine the regularization process within the MCI framework, enhancing its adaptability and effectiveness.

5.3 Expansion of MCI for 3D Surface Wave Imaging

Currently, approaches for constructing high-resolution 3D V_s models primarily rely on travel-time tomography (Fang et al., 2015; Cruz-Hernández et al., 2022; Xu et al., 2023) or waveform inversion (Sager et al., 2020; Pan et al., 2021). The developed MCI presents a promising alternative for 3D surface wave imaging. It can effectively address the challenging issues related to computational efficiency, robustness, and uncertainty estimation while achieving the necessary resolution.

Following the workflow outlined in Section 2.2.3 makes the realization of 3D MCI feasible. The key challenges in this expansion involve managing the collocated grid groups and addressing the additional intricacies of lateral variations. Although a similar multigrid parameterization strategy as in the 2D case can be employed in the 3D case, it requires the definition of a 3D base grid and collocated grids. Of particular importance is the establishment of the spatial gradient matrix ($\mathbf{D}$), which should encompass differential coefficients for 13 directions: three axial directions, six diagonal directions within the three 2D planes, and four 3D spatial diagonal directions.

6 Conclusions

We have developed a multigrid spatially constrained inversion (MCI) scheme for holistic inversion of dispersion curves to keep up with the increasing demands for high-resolution surface wave imaging in the context of Distributed Acoustic Sensing (DAS). Synthetic tests and a basin-scale field DAS case have demonstrated that MCI ensures inversion efficiency and robustness while concurrently enhancing imaging accuracy and spatial resolution. This is particularly noteworthy when compared to established dispersion curve inversion methods such as 1D Inversion (1DI) and Laterally Constrained Inversion (LCI) based on a 1D forward kernel. Additionally, MCI introduces a mechanism to evaluate the uncertainty associated with inversion results, providing a valuable reference for assessing the reliability of the constructed V_s model. Furthermore, MCI is recognized for its user-friendliness and adaptability to varying conditions.

We refined and constructed high spatial resolution V_s structures in Imperial Valley, by performing MCI on released open-source dispersion curves. Various methods for evaluating imaging quality consistently support the high reliability of the MCI inverted model. MCI provides improved constraints on the subsurface V_s structure in Imperial Valley, finely revealing potential shallow fault responses associated with deeper fault systems. This highlights its capability, in collaboration with DAS, to achieve large-scale, high spatial resolution surface wave imaging. Although this paper focused on the 2D case, the MCI approach can be easily extended to 3D without compromising its superiority.

The developed MCI offers a more efficient, stable, and high-resolution alternative to surface wave imaging methods based on a 1D forward framework.

Open Research

The raw dispersion curves from the 28 km DAS array are available in the following OSF repository: `https://osf.io/ckt9q` (Cheng, Ajo-Franklin, & Tribaldos, 2023). The refined 2D V_s models obtained in the field application can be found at Zenodo repository `https://doi.org/10.5281/zenodo.10047087`. All websites were last accessed in Nov 2023.

Acknowledgments

This project was supported by the Startup Funds of Zhejiang University. We thank the Imperial Valley Dark Fiber (IVDF) team for sharing the DAS data. We appreciate the useful discussion about multigrid parameterization with Dr. Song Luo.

References

Abd Rahman, N., Rehman, M. A., Zahari, N. A., Taib, A. M., Mohtar, W. H. M. W., Ramli, A. B., ... Nurddin, M. F. (2023). The potential of shear wave velocity as an erosion risk index. *Physics and Chemistry of the Earth, Parts A/B/C*, *129*, 103302.

Ajala, R., Persaud, P., Stock, J. M., Fuis, G. S., Hole, J. A., Goldman, M., & Scheirer, D. (2019). Three-dimensional basin and fault structure from a detailed seismic velocity model of coachella valley, southern california. *Journal of Geophysical Research: Solid Earth*, *124*(5), 4728–4750.

Ajo-Franklin, J., Dou, S., Lindsey, N., Monga, I., Tracy, C., Robertson, M., ... others (2019). Distributed acoustic sensing using dark fiber for near-surface characterization and broadband seismic event detection. *Scientific reports*, *9*(1), 1–14.

Ajo-Franklin, J., Rodríguez Tribaldos, V., Nayak, A., Cheng, F., Mellors, R., Chi, B., ... others (2022). The Imperial Valley Dark Fiber Project: Toward seismic studies using DAS and telecom infrastructure for geothermal applications. *Seismological Society of America*, *93*(5), 2906–2919.

Arato, A., Godio, A., & Sambuelli, L. (2014). Staggered grid inversion of cross hole 2-d resistivity tomography. *Journal of Applied Geophysics*, *107*, 60–70.

Auken, E., & Christiansen, A. V. (2004). Layered and laterally constrained 2d inversion of resistivity data. *Geophysics*, *69*(3), 752–761.

Ayres, A., & Theilen, F. (1999). Relationship between P-and S-wave velocities and geological properties of near-surface sediments of the continental slope of the Barents Sea. *Geophysical prospecting*, *47*(4), 431–441.

Bazin, S., Feuillet, N., Duclos, C., Crawford, W., Nercessian, A., Bengoubou-Valerius, M., ... Singh, S. (2010). The 2004–2005 Les Saintes (French West Indies) seismic aftershock sequence observed with ocean bottom seismometers. *Tectonophysics*, *489*(1-4), 91–103.

Beaty, K. S., Schmitt, D. R., & Sacchi, M. (2002). Simulated annealing inversion of multimode rayleigh wave dispersion curves for geological structure. *Geophysical Journal International*, *151*(2), 622–631.

Ben-Zion, Y., Vernon, F. L., Ozakin, Y., Zigone, D., Ross, Z. E., Meng, H., ... Barklage, M. (2015). Basic data features and results from a spatially dense seismic array on the San Jacinto fault zone. *Geophysical Journal International*, *202*(1), 370–380.

Bergamo, P., Dashwood, B., Uhlemann, S., Swift, R., Chambers, J. E., Gunn, D. A., & Donohue, S. (2016). Time-lapse monitoring of climate effects on earthworks

using surface waves. *Geophysics*, *81*(2), EN1–EN15.

Bottelin, P., Jongmans, D., Baillet, L., Lebourg, T., Hantz, D., Lévy, C., ... others (2013). Spectral analysis of prone-to-fall rock compartments using ambient vibrations. *Journal of Environmental and Engineering Geophysics*, *18*(4), 205–217.

Cercato, M. (2007). Computation of partial derivatives of rayleigh-wave phase velocity using second-order subdeterminants. *Geophysical Journal International*, *170*(1), 217–238.

Cercato, M. (2009). Addressing non-uniqueness in linearized multichannel surface wave inversion. *Geophysical Prospecting*, *57*(1), 27–47.

Chen, X. (1993). A systematic and efficient method of computing normal modes for multilayered half-space. *Geophysical Journal International*, *115*(2), 391–409.

Cheng, F., Ajo-Franklin, J., Nayak, A., Rodriguez Tribaldos, V., & the Imperial Valley Dark Fiber Team. (2023). Using dark fiber and distributed acoustic sensing to characterize a geothermal system in the imperial valley, southern california. *Journal of Geophysical Research: Solid Earth*, *128*, e2022JB025240. doi: 10.1029/2022JB025240

Cheng, F., Ajo-Franklin, J. B., & Tribaldos, V. R. (2023). High-resolution near-surface imaging at the basin scale using dark fiber and distributed acoustic sensing: Towards site effect estimation in urban environments. *Journal of Geophysical Research: Solid Earth*, e2023JB026957.

Cheng, F., Chi, B., Lindsey, N., Dawe, C., & Ajo-Franklin, J. (2021b). Utilizing distributed acoustic sensing and ocean bottom fiber optic cables for submarine structural characterization. *Scientific Reports*, *11*(1), 5613. doi: 10.1038/s41598-021-84845-y

Cheng, F., Lindsey, N. J., Sobolevskaia, V., Dou, S., Freifeld, B., Wood, T., ... Ajo-Franklin, J. B. (2022). Watching the cryosphere thaw: Seismic monitoring of permafrost degradation using distributed acoustic sensing during a controlled heating experiment. *Geophysical Research Letters*, *49*(10), e2021GL097195.

Cheng, F., Xia, J., Ajo-Franklin, J. B., Behm, M., Zhou, C., Dai, T., ... Zhou, C. (2021a). High-resolution ambient noise imaging of geothermal reservoir using 3c dense seismic nodal array and ultra-short observation. *Journal of Geophysical Research: Solid Earth*, *126*(8), e2021JB021827.

Cruz-Hernández, F., Gallardo, L. A., Calò, M., Castro, R. R., & Romo-Jones, J. M. (2022). Laterally constrained surface wave inversion. *Geophysical Journal International*, *230*(2), 1121–1131.

Dokht Dolatabadi Esfahani, R., Gholami, A., & Ohrnberger, M. (2020). An inexact augmented lagrangian method for nonlinear dispersion-curve inversion using dix-type global linear approximation. *Geophysics*, *85*(5), EN77–EN85.

Fang, H., Yao, H., Zhang, H., Huang, Y.-C., & van der Hilst, R. D. (2015). Direct inversion of surface wave dispersion for three-dimensional shallow crustal structure based on ray tracing: methodology and application. *Geophysical Journal International*, *201*(3), 1251–1263. Retrieved from `https://doi.org/10.1093/gji/ggv080` doi: 10.1093/gji/ggv080

Farquharson, C. G. (2008). Constructing piecewise-constant models in multidimensional minimum-structure inversions. *Geophysics*, *73*(1), K1–K9.

Foti, S., Comina, C., Boiero, D., & Socco, L. (2009). Non-uniqueness in surface-wave inversion and consequences on seismic site response analyses. *Soil Dynamics and Earthquake Engineering*, *29*(6), 982–993.

Foti, S., Parolai, S., Albarello, D., & Picozzi, M. (2011). Application of surface-wave methods for seismic site characterization. *Surveys in geophysics*, *32*(6), 777–825.

Frith, R. B. (1978). *Seismic refraction investigation of the Salton Sea geothermal area, Imperial Valley, California* (Tech. Rep.). California Univ., Riverside (USA). Retrieved from `https://www.osti.gov/servlets/purl/5716342`

Golub, G. H., & Van Loan, C. F. (2013). *Matrix computations*. JHU press.

Guan, J., Li, Y., Ji, R., Liu, G., & Yan, Y. (2022). Love wave full-waveform inversion for archaeogeophysics: From synthesis tests to a field case. *Journal of Applied Geophysics*, *202*, 104653.

Guillemoteau, J., Vignoli, G., Barreto, J., & Sauvin, G. (2022). Sparse laterally constrained inversion of surface-wave dispersion curves via minimum gradient support regularization. *Geophysics*, *87*(3), R281–R289.

Haney, M. M., & Qu, L. (2010). Rayleigh wave dispersion curve inversion: Occam versus the l1-norm. In *Seg technical program expanded abstracts 2010* (pp. 1871–1876). Society of Exploration Geophysicists.

Haskell, N. (1953). The dispersion of surface waves on multilayered media. *The Bulletin of the Seismological Society of America*, *43*(1), 17–34.

Herrmann, R. B., & Ammon, C. J. (2002). Computer programs in seismology: Surface waves, receiver functions and crustal structure. *St. Louis University, St. Louis, MO*, *25*, 46.

Hu, S., Zhao, Y., Socco, L. V., & Ge, S. (2021). Retrieving 2-D laterally varying structures from multistation surface wave dispersion curves using multiscale window analysis. *Geophysical Journal International*, *227*(2), 1418–1438. Retrieved from `https://doi.org/10.1093/gji/ggab282` doi: 10.1093/gji/ggab282

Jackson, D. D. (1981). *Seismic and geodetic studies of the Imperial Valley, California* (Tech. Rep.). Lawrence Livermore National Lab., CA (USA) and California Univ., Los Angeles.

Kanbur, M. Z., Silahtar, A., & Aktan, G. (2020). Local site effects evaluation by surface wave and H/V survey methods in senirkent (isparta) region, southwestern turkey. *Earthquake Engineering and Engineering Vibration*, *19*, 321–333.

Kaspereit, D., Mann, M., Sanyal, S., Rickard, B., Osborn, W., & Hulen, J. (2016). Updated conceptual model and reserve estimate for the Salton Sea geothermal field, Imperial Valley, California. *Geotherm. Res. Council Trans*, *40*, 57–66.

Knopoff, L. (1964). A matrix method for elastic wave problems. *Bulletin of the Seismological Society of America*, *54*(1), 431–438.

Kühn, D., Ohrnberger, M., & Dahm, T. (2011). Imaging a shallow salt diapir using ambient seismic vibrations beneath the densely built-up city area of Hamburg, Northern Germany. *Journal of seismology*, *15*, 507–531.

Li, J., Feng, Z., & Schuster, G. (2017). Wave-equation dispersion inversion. *Geophysical Journal International*, *208*(3), 1567–1578. doi: 10.1093/gji/ggw465

Li, J., Hanafy, S., & Schuster, G. (2018). Wave-equation dispersion inversion of guided P waves in a waveguide of arbitrary geometry. *Journal of Geophysical Research: Solid Earth*, *123*(9), 7760–7774.

Lin, C.-P., & Lin, C.-H. (2007). Effect of lateral heterogeneity on surface wave testing: Numerical simulations and a countermeasure. *Soil Dynamics and Earthquake Engineering*, *27*(6), 541–552.

Lindsey, N. J., Dawe, T. C., & Ajo-Franklin, J. B. (2019). Illuminating seafloor faults and ocean dynamics with dark fiber distributed acoustic sensing. *Science*, *366*(6469), 1103–1107. doi: 10.1126/science.aay5881

Lindsey, N. J., Martin, E. R., Dreger, D. S., Freifeld, B., Cole, S., James, S. R., ... Ajo-Franklin, J. B. (2017). Fiber-optic network observations of earthquake wavefields. *Geophysical Research Letters*, *44*(23), 11–792.

Liu, H., Li, J., & Wang, Y. (2022). Wave Equation Dispersion Inversion of Distributed Acoustic Sensing Data. *Journal of Geophysical Research: Solid Earth*, *127*(11), e2022JB024671. doi: 10.1029/2022JB024671

Liu, Y., Wei, X., Liu, Q., & Chen, X. (2023). Double-source frequency–wavenumber transform for accurate extraction of 2-d media dispersion. *Geophysical Journal International*, *235*(1), 74–93. Retrieved from `https://doi.org/10.1093/gji/ggad208` doi: 10.1093/gji/ggad208

Luo, S., Yao, H., Wang, J., Wang, K., & Liu, B. (2021). Direct inversion of surface wave dispersion data with multiple-grid parametrizations and its application to a dense array in Chao Lake, eastern China. *Geophysical Journal International*, *225*(2), 1432–1452.

Mecking, R., Köhn, D., Meinecke, M., & Rabbel, W. (2021). Cavity detection by sh-wave full-waveform inversion—a reflection-focused approach. *Geophysics*, *86*(3), WA123–WA137.

Meidav, T., & Furgerson, R. (1972). Resistivity studies of the Imperial Valley geothermal area, California. *Geothermics*, *1*(2), 47–62.

Mi, B., Xia, J., Bradford, J. H., & Shen, C. (2020). Estimating Near-Surface Shear-Wave-Velocity Structures Via Multichannel Analysis of Rayleigh and Love Waves: An Experiment at the Boise Hydrogeophysical Research Site. *Surveys in Geophysics*, *41*(2), 323–341.

Mi, B., Xia, J., Shen, C., Wang, L., Hu, Y., & Cheng, F. (2017). Horizontal resolution of multichannel analysis of surface waves. *GEOPHYSICS*, *82*(3), EN51–EN66. Retrieved from `https://doi.org/10.1190/geo2016-0202.1` doi: 10.1190/geo2016-0202.1

Pan, Y., Gao, L., & Bohlen, T. (2021). Random-objective waveform inversion of 3D-9C shallow-seismic field data. *Journal of Geophysical Research: Solid Earth*, *126*(9), e2021JB022036.

Park, C. B., & Miller, R. D. (2008). Roadside passive multichannel analysis of surface waves (MASW). *Journal of Environmental and Engineering Geophysics*, *13*(1), 1–11. Retrieved from `https://doi.org/10.2113/jeeg13.1.1` doi: 10.2113/jeeg13.1.1

Parker, T., Shatalin, S., & Farhadiroushan, M. (2014). Distributed Acoustic Sensing–a new tool for seismic applications. *first break*, *32*(2).

Persaud, P., Ma, Y., Stock, J. M., Hole, J. A., Fuis, G. S., & Han, L. (2016). Fault zone characteristics and basin complexity in the southern Salton Trough, California. *Geology*, *44*(9), 747–750.

Porcella, R. L. (1984). *Geotechnical investigations at strong-motion stations in the imperial valley, california* (Tech. Rep.). US Department of the Interior, Geological Survey. Retrieved from `https://pubs.usgs.gov/of/1984/0562/report.pdf`

Portniaguine, O., & Zhdanov, M. S. (1999). Focusing geophysical inversion images. *Geophysics*, *64*(3), 874–887.

Posey Jr, R., Johnson, G., & Vohra, S. (2000). Strain sensing based on coherent rayleigh scattering in an optical fibre. *Electronics Letters*, *36*(20), 1.

Rodríguez Tribaldos, V., & Ajo-Franklin, J. B. (2021). Aquifer monitoring using ambient seismic noise recorded with distributed acoustic sensing (DAS) deployed on dark fiber. *Journal of Geophysical Research: Solid Earth*, *126*(4), e2020JB021004.

Sager, K., Boehm, C., Ermert, L., Krischer, L., & Fichtner, A. (2020). Global-scale full-waveform ambient noise inversion. *Journal of Geophysical Research: Solid Earth*, *125*(4), e2019JB018644.

Salas-Romero, S., Malehmir, A., Snowball, I., & Brodic, B. (2021). Geotechnical site characterization using multichannel analysis of surface waves: A case study of an area prone to quick-clay landslides in southwest sweden. *Near Surface Geophysics*, *19*(6), 699–715.

Sambridge, M. (1999). Geophysical inversion with a neighbourhood algorithm—i. searching a parameter space. *Geophysical Journal International*, *138*(2), 479–494. Retrieved from `https://doi.org/10.1046/j.1365-246x.1999.00876.x` doi: 10.1046/j.1365-246x.1999.00876.x

Sawayama, K., Ikeda, T., Tsuji, T., Jiang, F., Nishizawa, O., & Fujimitsu, Y. (2022). Elastic wave velocity changes due to the fracture aperture and density, and direct correlation with permeability: an energetic approach to mated rock frac-

tures. *Journal of Geophysical Research: Solid Earth*, *127*(2), e2021JB022639.

Sens-Schönfelder, C., & Wegler, U. (2006). Passive image interferometry and seasonal variations of seismic velocities at merapi volcano, indonesia. *Geophysical research letters*, *33*(21).

Shapiro, N. M., & Ritzwoller, M. H. (2002). Monte-carlo inversion for a global shear-velocity model of the crust and upper mantle. *Geophysical Journal International*, *151*(1), 88–105. Retrieved from `https://doi.org/10.1046/j.1365-246x.2002.01742.x` doi: 10.1046/j.1365-246x.2002.01742.x

Shi, Y., & Jin, W. (1995). Genetic algorithms inversion of lithospheric structure from surface wave dispersion. In *Chinese science abstracts series b* (Vol. 4, p. 58).

Socco, L. V., Boiero, D., Foti, S., & Wisén, R. (2009). Laterally constrained inversion of ground roll from seismic reflection records. *Geophysics*, *74*(6), G35–G45.

Song, X., Tang, L., Lv, X., Fang, H., & Gu, H. (2012). Application of particle swarm optimization to interpret rayleigh wave dispersion curves. *Journal of Applied Geophysics*, *84*, 1–13.

Song, Z., Zeng, X., Xu, S., Hu, J., Sun, T., & Wang, B. (2020). Distributed acoustic sensing for imaging shallow structure i: active source survey. *Chinese Journal of Geophysics*, *63*(2), 532–540.

Spica, Z. J., Nishida, K., Akuhara, T., Pétrélis, F., Shinohara, M., & Yamada, T. (2020). Marine sediment characterized by ocean-bottom fiber-optic seismology. *Geophysical Research Letters*, *47*(16), e2020GL088360.

Strobbia, C., & Foti, S. (2006). Multi-offset phase analysis of surface wave data (mopa). *Journal of Applied Geophysics*, *59*(4), 300–313.

Thurber, C. H. (1983). Earthquake locations and three-dimensional crustal structure in the Coyote Lake area, central California. *Journal of Geophysical Research: Solid Earth*, *88*(B10), 8226–8236.

Tikhonov, A. N. (1963). On the solution of ill-posed problems and the method of regularization. In *Doklady akademii nauk* (Vol. 151, pp. 501–504).

Tong, P., Yang, D., & Huang, X. (2019). Multiple-grid model parametrization for seismic tomography with application to the San Jacinto fault zone. *Geophysical Journal International*, *218*(1), 200–223.

Towse, D. (1975). *An estimate of the geothermal energy resource in the Salton Trough, California. UCRL-51851 (Rev.1).* (Tech. Rep.). California Univ., Livermore (USA). Lawrence Livermore Lab. Retrieved from `https://www.osti.gov/biblio/7353985`

Vesnaver, A., & Böhm, G. (2000). Staggered or adapted grids for seismic tomography? *The Leading Edge*, *19*(9), 944–950.

Vignoli, G., Cassiani, G., Rossi, M., Deiana, R., Boaga, J., & Fabbri, P. (2012). Geophysical characterization of a small pre-Alpine catchment. *Journal of Applied Geophysics*, *80*, 32–42.

Vignoli, G., Guillemoteau, J., Barreto, J., & Rossi, M. (2021). Reconstruction, with tunable sparsity levels, of shear wave velocity profiles from surface wave data. *Geophysical Journal International*, *225*(3), 1935–1951.

Walter, F., Gräff, D., Lindner, F., Paitz, P., Köpfli, M., Chmiel, M., & Fichtner, A. (2020). Distributed acoustic sensing of microseismic sources and wave propagation in glaciated terrain. *Nature communications*, *11*(1), 1–10.

Wang, T., Guan, J., Yang, Z., He, X., Peng, L., Yan, Y., & Cui, S. (2023). Utility tunnel detection by 2D elastic PSV/Rayleigh-wave multi-parameter full waveform inversion. *Journal of Applied Geophysics*, 105087.

Wathelet, M., Jongmans, D., & Ohrnberger, M. (2004). Surface-wave inversion using a direct search algorithm and its application to ambient vibration measurements. *Near Surface Geophysics*, *2*(4), 211–221.

Wisén, R., & Christiansen, A. V. (2005). Laterally and mutually constrained inver-

sion of surface wave seismic data and resistivity data. *Journal of Environmental & Engineering Geophysics*, *10*(3), 251–262.

Xia, J. (2014). Estimation of near-surface shear-wave velocities and quality factors using multichannel analysis of surface-wave methods. *Journal of applied geophysics*, *103*, 140–151.

Xia, J., Miller, R. D., & Park, C. B. (1999). Estimation of near-surface shear-wave velocity by inversion of rayleigh waves. *Geophysics*, *64*(3), 691–700.

Xu, W., Ding, Z., Wu, P., Lu, L., & Qin, T. (2023). Improved 3D Shallow-Deep Vs Structure in Tongzhou, Beijing (China), Revealed by Dense Array Ambient Noise Tomography. *Earth and Space Science*, *10*(5), e2022EA002707.

Yan, Y., Chen, X., Li, J., Guan, J., Xi, C., & Liu, H. (2023). Inversion of multimodal dispersion curves from distributed acoustic sensing measurements for subsurface imaging: A field case of Garner Valley, California. *Journal of Applied Geophysics*, 105070.

Zhang, C., Li, J., Yu, H., & Liu, B. (2023). Autoencoded elastic wave-equation traveltime inversion: Toward reliable near-surface tomogram. *IEEE Transactions on Geoscience and Remote Sensing*, *61*, 1–13. Retrieved from `https://doi.org/10.1109/tgrs.2023.3243140` doi: 10.1109/tgrs.2023.3243140

Zhdanov, M. S. (2002). *Geophysical inverse theory and regularization problems* (Vol. 36). Elsevier.

Table 1. Grid groups associated to synthetic tests.

Grid Classification	**Layer thickness** (m)	**Grid index**	**Grid group**
Base grid	1	$s0$	$\{s0\}$
Collocated grid	$1 \sim 2$	s1	$\{s1\}$
Collocated grid	$1.3 \sim 2.6$	s2	$\{s2\}$
Collocated grid	$1.6 \sim 2.9$	s3	$\{s3\}$
Collocated grid	$1.9 \sim 3.8$	s4	$\{s4\}$
Multiple grids	–	s5	$\{s1, s2, s3, s4\}$
Multiple grids	–	s6	$\{s1, s2\}$
Multiple grids	–	s7	$\{s2, s3\}$
Multiple grids	–	s8	$\{s3, s4\}$
Multiple grids	–	s9	$\{s1, s2, s3\}$
Multiple grids	–	s10	$\{s2, s3, s4\}$

Table 2. Grid groups associated to field application.

Grid Classification	**Layer thickness**(m)	**Grid index**	**Grid group**
Base grid	1	$f0$	$\{f0\}$
Collocated grid	$1 \sim 3$	$f1$	$\{f1\}$
Collocated grid	$1 \sim 4$	$f2$	$\{f2\}$
Collocated grid	$1 \sim 5$	$f3$	$\{f3\}$
Collocated grid	$1 \sim 6$	$f4$	$\{f4\}$
Multiple grids	–	$f5$	$\{f1, f2, f3, f4\}$

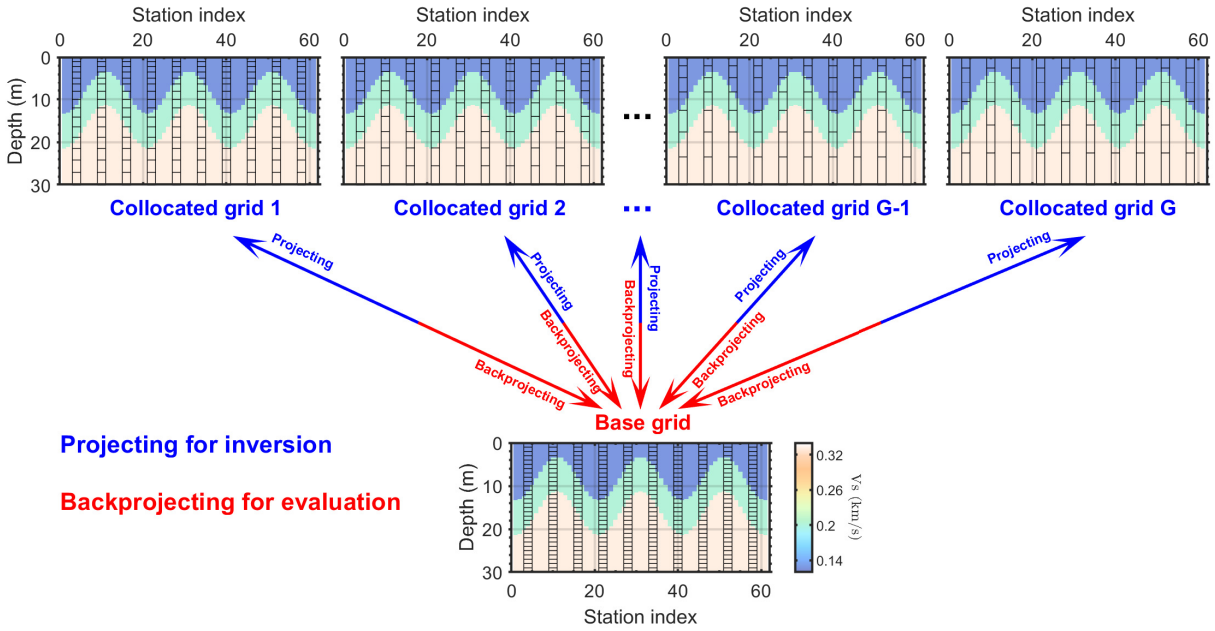

Figure 1. Multigrid strategy schematic.

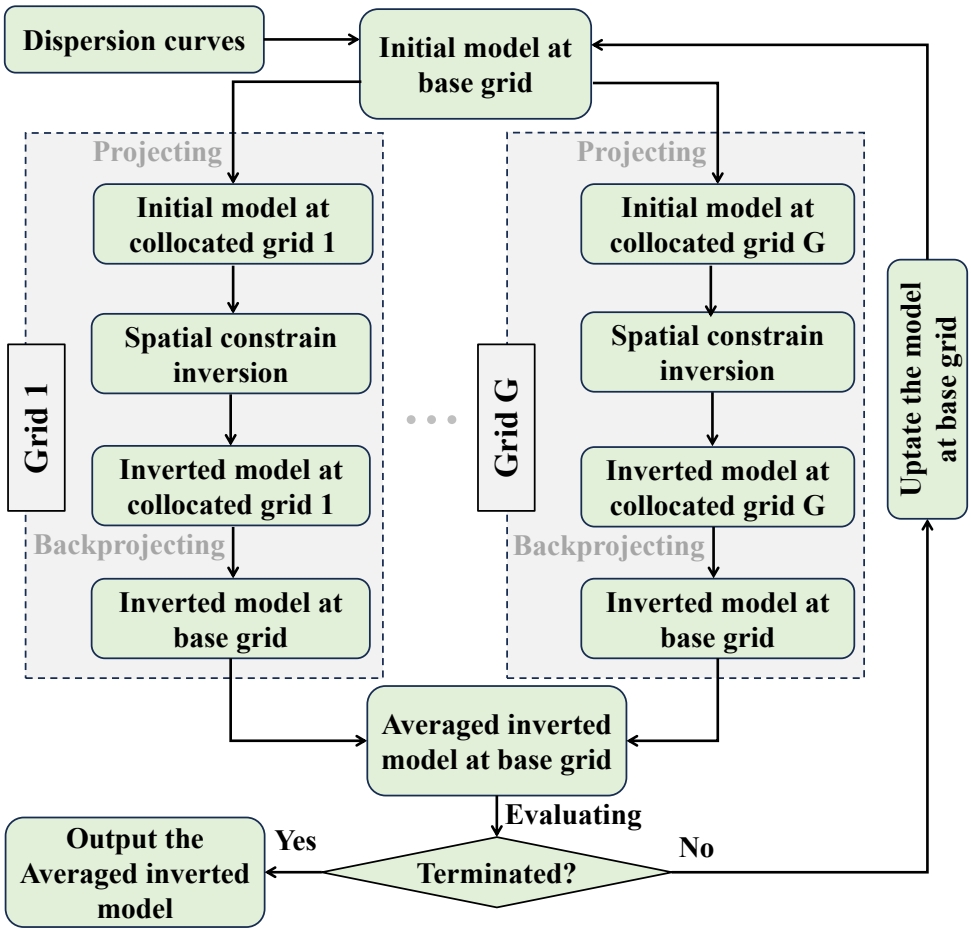

Figure 2. The workflow of multigrid spatially constrained inversion scheme.

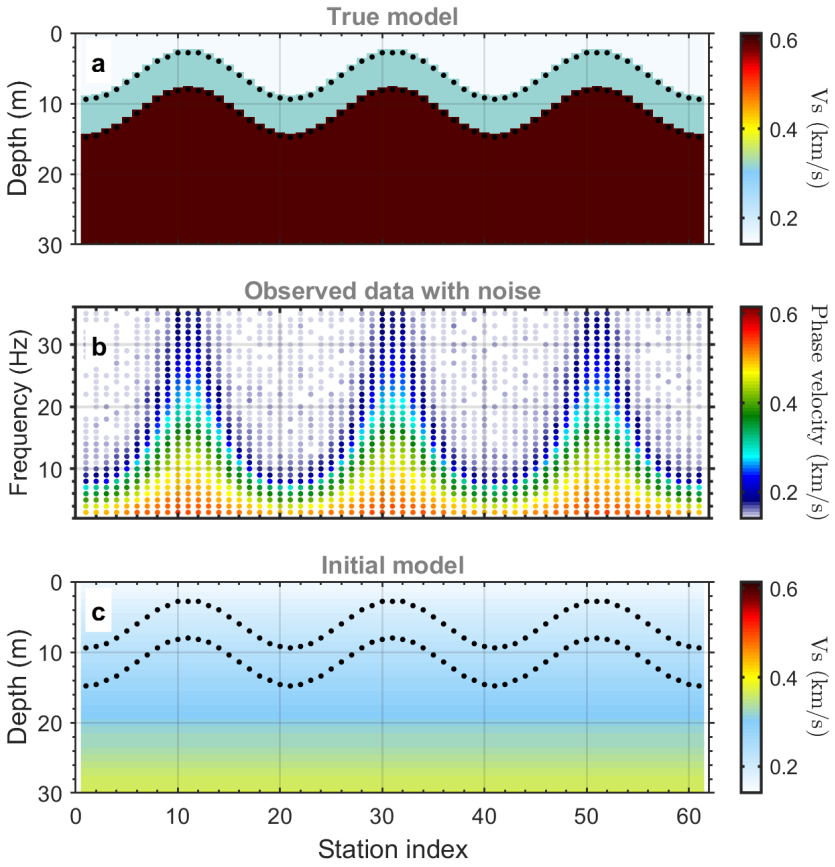

Figure 3. Models and dispersion data in synthetic test. (a) The true model is a pseudo-2D model composed of 61 horizontally-aligned 1D models. (b) 2D phase velocity distribution synthesized with the model shown in (a), but with 4% Gaussian white noise added. (c) The established initial layered gradient model. The black dotted lines in (a) and (c) represent the layer interfaces.

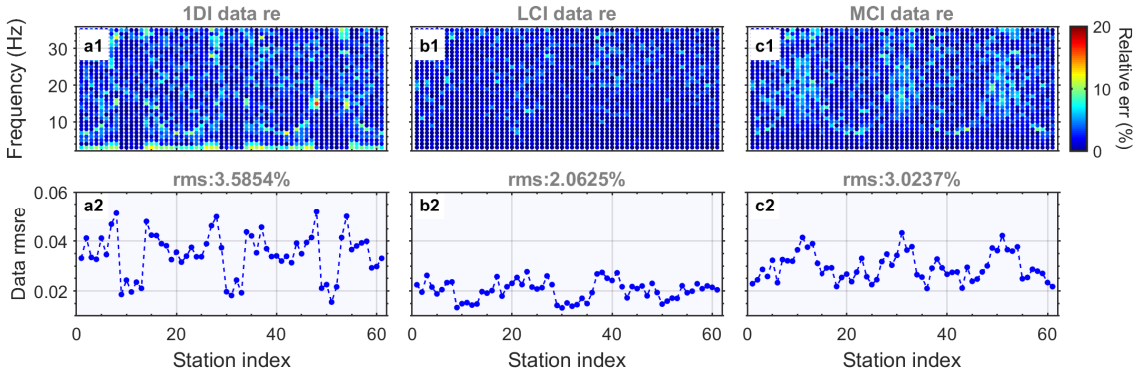

Figure 4. The data residual of 1DI (the left panels), LCI (the middle panels), and MCI (the right panels) in the synthetic test. The top panels display the relative error of each dispersion data point (a1, b1, c1), and the bottom panels depict the root-mean-square relative error of dispersion data for each station (a2, b2, c2). Here we define the relative data error with $\frac{|\mathbf{d}-\mathbf{d}_{pre}|}{\mathbf{d}} * 100\%$, where $\mathbf{d}$ and $\mathbf{d}_{pre}$ represents the observed and predicted data, respectively.

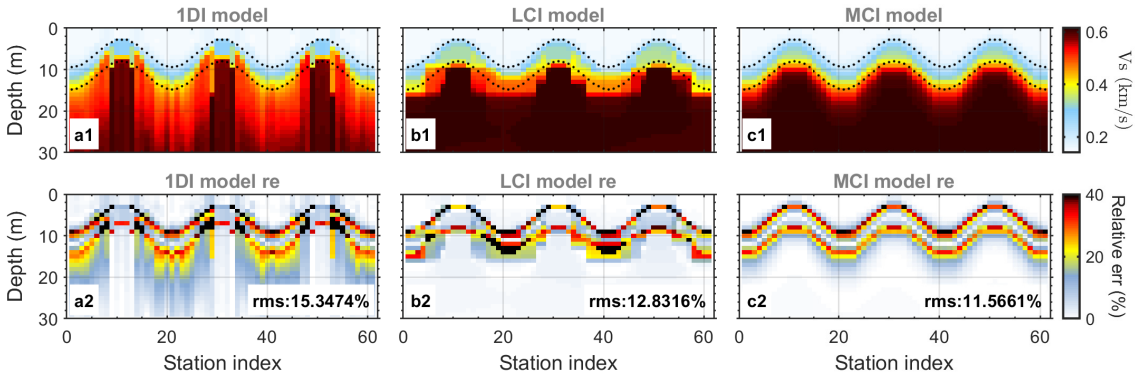

Figure 5. The inversion results of 1DI (the left panels), LCI (the middle panels), and MCI (the right panels) in the synthetic test. The top panels display the inverted models (a1, b1, c1), and the bottom panels depict the relative error of inverted V_s for each model cell (a2, b2, c2). Here we define the relative model error with $\frac{|\mathbf{m}_{true}-\mathbf{m}_{inv}|}{\mathbf{m}_{true}} * 100\%$, where $\mathbf{m}_{true}$ and $\mathbf{m}_{inv}$ represent the true and inverted model, respectively.

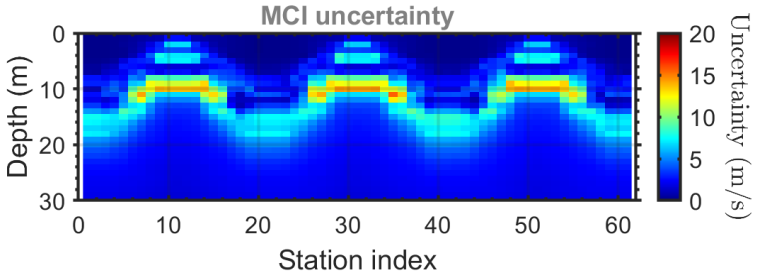

Figure 6. The estimated uncertainty of the inverted model by MCI in the synthetic test.

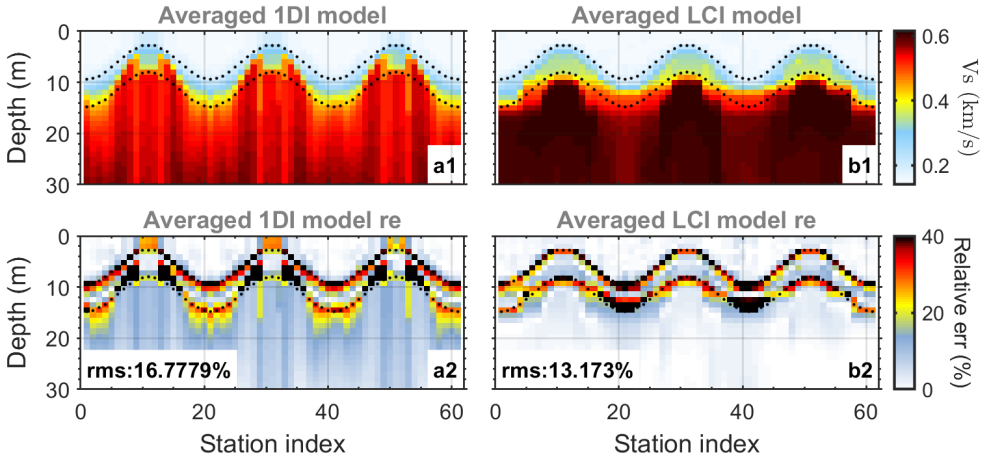

Figure 7. The averaged inversion results from four collocated grids (Grid s1 - Grid s4) using 1DI (the left panels) and LCI (the right panels), respectively. The top panels dispaly the averaged inverted results (a1, b1), and the bottom panels depict the relative error of averaged inverted V_s for each model cell (a2, b2). The black dotted lines in (a1) and (b1) indicate the layer interfaces.

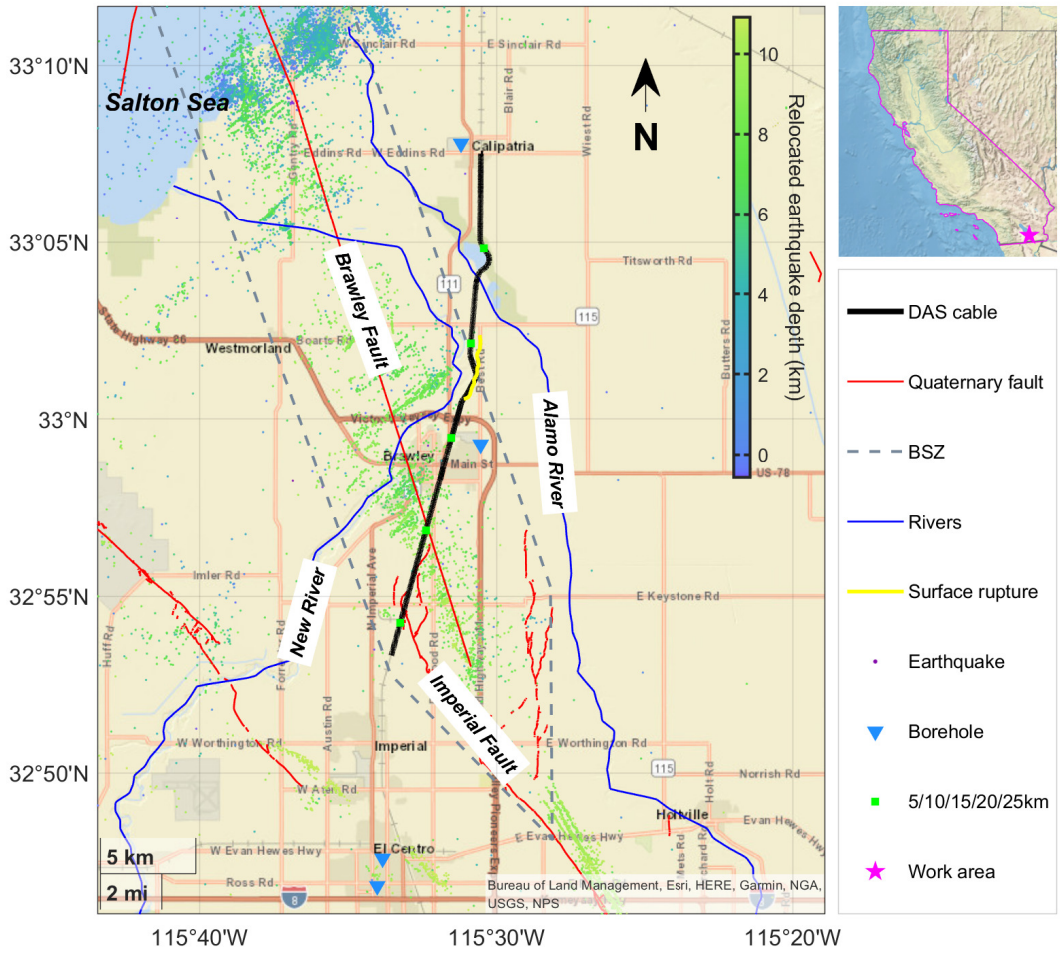

Figure 8. Overview of the DAS field experiment area. The black line traces the approximately 28 km of DAS cable utilized in the experiment. Green squares, evenly spaced between 5 and 25 km from north to south, mark key locations. Light blue inverted triangles pinpoint four borehole survey sites. Noteworthy features include the representation of quaternary fault networks (red lines), two rivers (blue lines), and a surface rupture due to the 2012 Brawley swarm (yellow line). The grey dashed line encircles the Brawley seismic zone. Historical seismic events are depicted by depth-coded dots in shades of purple to light green.

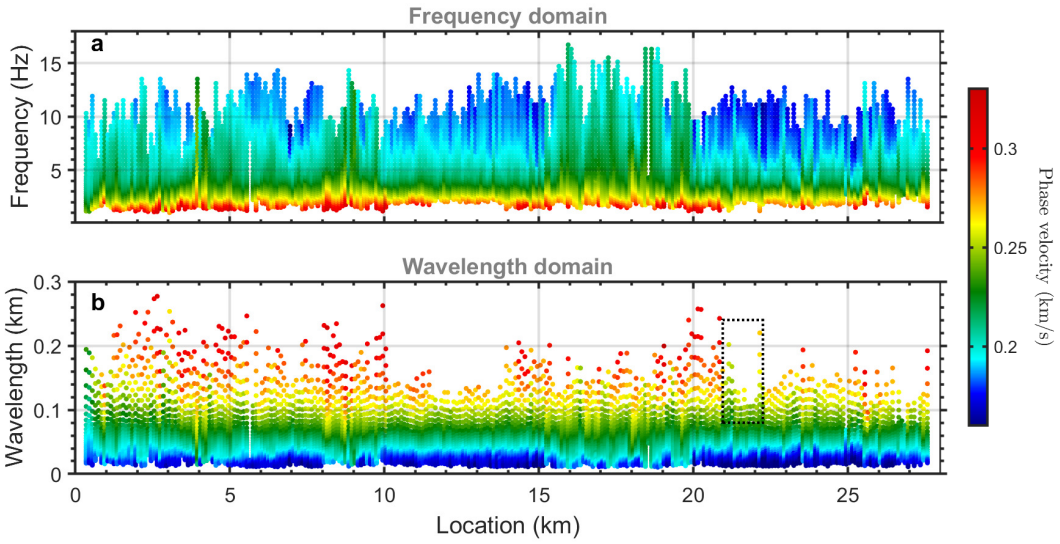

Figure 9. Presentation of 273 fundamental-mode dispersion curves in the frequency domain (a) and wavelength domain (b), as employed in the field application. The black dashed box delineates an area characterized by potentially strong lateral discontinuity, exceeding a length of 1 km.

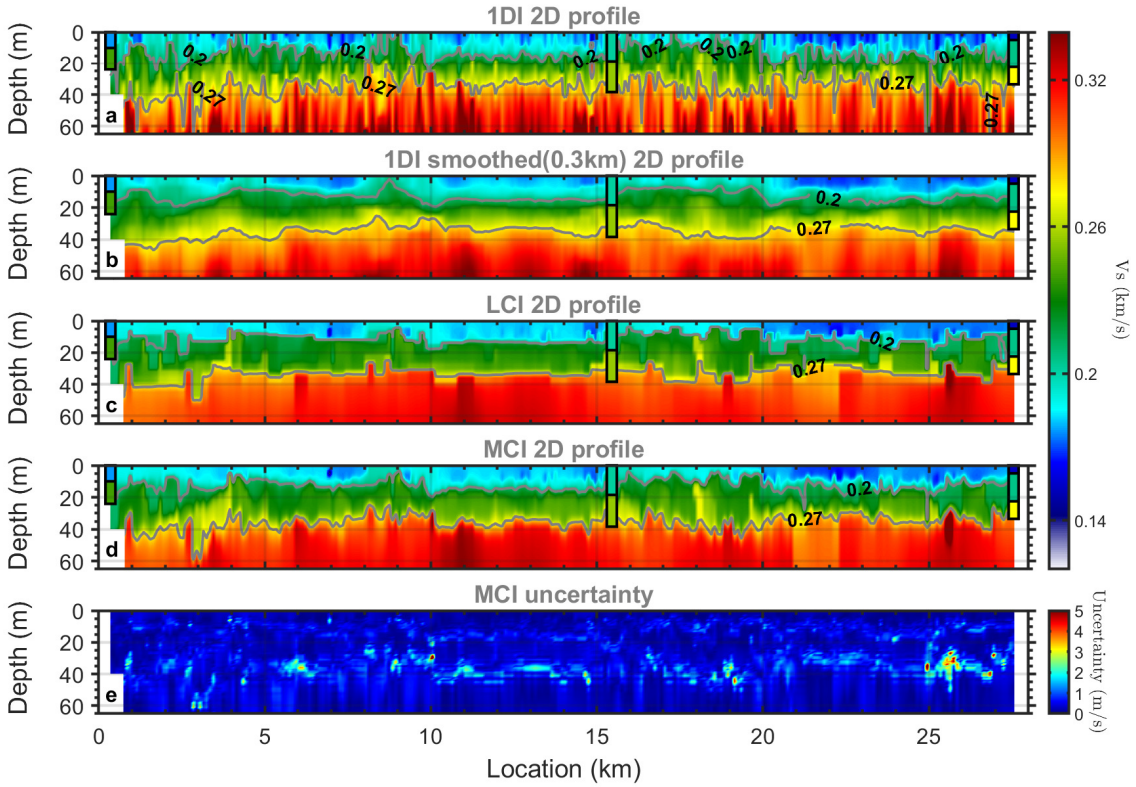

Figure 10. The near-surface 2D V_s structures in the Imperial Valley inverted by different methods. Panels (a)-(b) show the inverted model of 1DI and its smoothed version. Panel (c) displays the inverted model obtained through LCI. Panels (d)-(e) present the inverted model of MCI and its corresponding model uncertainty. Results from both 1DI and LCI are based on Grid f1. In panels (a)-(d), two gray lines depict the variation of depth along the DAS cable for velocity contour lines of 200 m/s and 270 m/s. Colored sticks overlaid on the 2D inverted profiles represent three nearby borehole profiles.

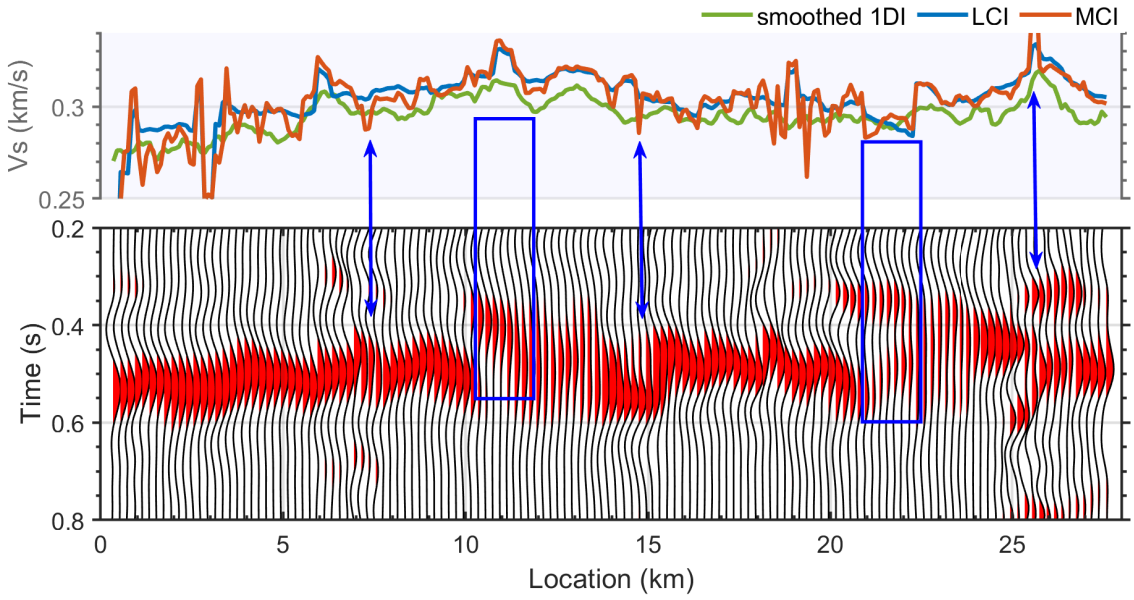

Figure 11. Lateral variations in the underground structure beneath the DAS cable. Panel (a) presents V_s profiles at a depth of 45 m, extracted from three inverted models in Fig. 10b-d. Panel (b) displays the common offset profile at an offset of 84 m, filtered by the 1-9 Hz bandpass. The deep blue arrows and boxes highlight the area where MCI demonstrates greater consistency in the lateral changes between the V_s profile (orange curve) and the common offset profile.

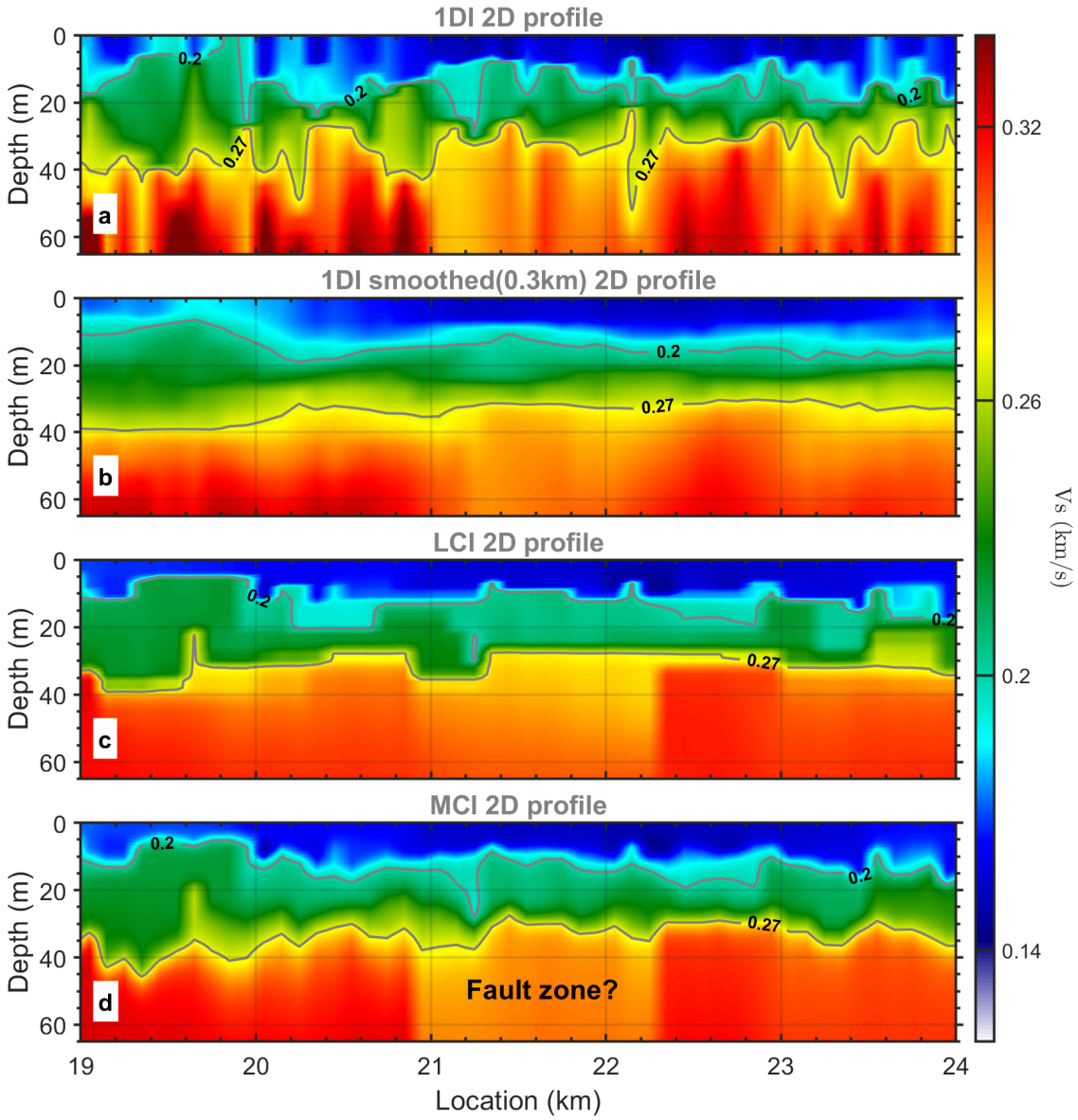

Figure 12. Segmented views (partitions: 19 km - 24 km) of different inverted models represented in Fig. 10a-d.

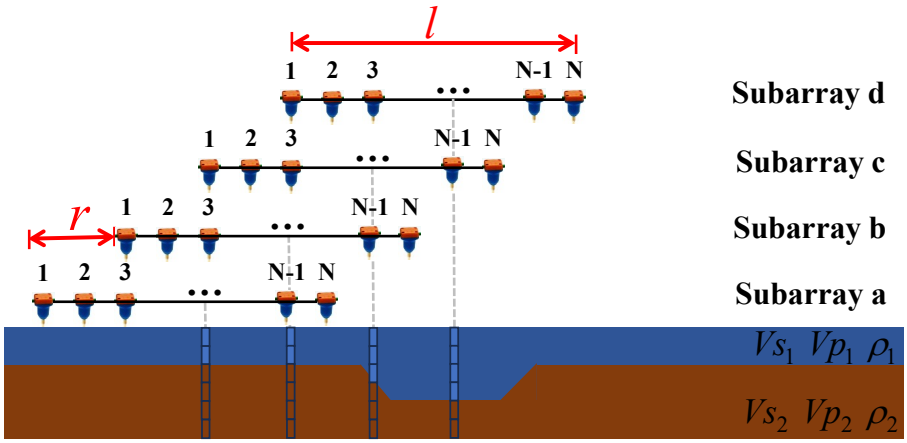

Figure 13. Characterization of subsurface structure by means of multichannel analysis of surface waves and the rolling-along data acquisition strategy. r and l represent the subarray rolling distance and the subarray spread length. The colored sticks represent the 1D profiles unveiled by different subarrays.

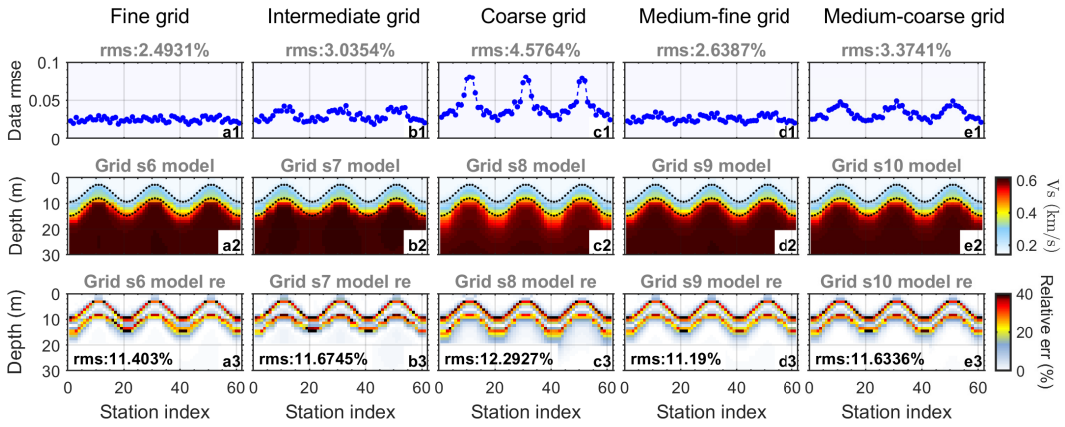

Figure 14. MCI inversion results using various grid groups, Grid s6 (fine grid), Grid s7 (intermediate grid), Grid s8 (coarse grid), Grid s9 (Medium-fine grid), Grid s10 (medium-coarse grid). Each panel includes, from top to bottom, the root-mean-square relative error of dispersion data for each station (a1, b1, c1, d1, e1), the inverted 2D V_s model (a2, b2, c2, d2, e2), and the relative model residual at each discrete grid point (a3, b3, c3, d3, e3). The black dotted lines in a2, b2, c2, d2, e2 represent the layer interfaces.